

Computational Design of Transmembrane Pores

Chunfu Xu^{1,2,3,12}, **Peilong Lu**^{1,2,4,5,12,*}, **Tamer M. Gamal El-Din**⁶, **Xue Y. Pei**⁷, **Matthew C. Johnson**², **Atsuko Uyeda**⁸, **Matthew J. Bick**^{1,2,10}, **Qi Xu**^{4,5}, **Daohua Jiang**⁶, **Hua Bai**^{1,2}, **Gabriella Reggiano**^{1,2}, **Yang Hsia**^{1,2}, **TJ Brunette**^{1,2}, **Jiayi Dou**^{1,2,11}, **Dan Ma**^{4,5,9}, **Eric Lynch**², **Scott E. Boyken**^{1,2,10}, **Po-Ssu Huang**^{1,2,11}, **Lance Stewart**¹, **Frank DiMaio**^{1,2}, **Justin M. Kollman**², **Ben F. Luisi**⁷, **Tomoaki Matsuura**⁸, **William A. Catterall**⁶, **David Baker**^{1,2,3,*}

¹Institute for Protein Design, University of Washington, Seattle, WA 98195, USA

²Department of Biochemistry, University of Washington, Seattle, WA 98195, USA

³Howard Hughes Medical Institute, University of Washington, Seattle, WA 98195, USA

⁴Key Laboratory of Structural Biology of Zhejiang Province, School of Life Sciences, Westlake University, 18 Shilongshan Road, Hangzhou 310024, Zhejiang Province, China

⁵Institute of Biology, Westlake Institute for Advanced Study, 18 Shilongshan Road, Hangzhou 310024, Zhejiang Province, China

⁶Department of Pharmacology, University of Washington, Seattle, WA 98195, USA

⁷Department of Biochemistry, University of Cambridge, Cambridge CB2 1GA, UK

⁸Department of Biotechnology, Graduate School of Engineering, Osaka University, Suita, Osaka 565-0871, Japan

⁹Department of Biological Structure, University of Washington, Seattle, WA, USA

¹⁰Present address: Lyell Immunopharma, Inc., Seattle, WA, USA

¹¹Present address: Department of Bioengineering, Stanford University, Stanford, CA, USA

¹²These authors contributed equally to this manuscript: Chunfu Xu, Peilong Lu

Abstract

Users may view, print, copy, and download text and data-mine the content in such documents, for the purposes of academic research, subject always to the full Conditions of use:http://www.nature.com/authors/editorial_policies/license.html#terms

* lupeilong@westlake.edu.cn; dabaker@uw.edu.

Author Contributions

C.X., P.L., T.M.G., L.S., T.M., W.A.C. and D.B. planned the research and designed experiments. C.X., P.L., and D.B. designed the proteins. C.X., P.L., T.M.G., J.D., T.M., W.A.C. D.B. wrote the manuscript. C.X. and P.L. carried out biophysical characterizations. T.M.G. and W.A.C. performed patch-clamp experiments and analysed data. A.U. and T.M. performed liposome permeability assays and analysed data. X.Y.P., M.J.B., and B.F.L. solved crystal structures. P.L., Q.X., M.C.J., J.M.K. determined the cryoEM structure. G.R. and F.D. refined the cryoEM structure. J.D. carried out the yeast growth assay. D.J. and D.M. prepared samples for patch-clamp experiments. E.L. took negatively stained electron micrographs. H.B., Y.H., T.J.B., S.E.B., and P.S.H. helped with design calculations. All authors discussed the results and commented on the manuscript.

Competing Interests

C.X., P.L., T.M.G., W.A.C., and D.B. are inventors on a U.S. provisional patent application (63/017,810) submitted by the University of Washington that covers the computational design of transmembrane pores described in this paper.

Protein pores play key roles in fundamental biological processes¹ and biotechnological applications such as DNA nanopore sequencing²⁻⁴, and hence the design of pore-containing proteins is of considerable scientific and biotechnological interest. Synthetic amphiphilic peptides have been found to form ion channels^{5,6}, and there have been recent advances in *de novo* membrane protein design^{7,8} and in redesigning naturally occurring channel-containing proteins^{9,10}. However, the *de novo* design of stable, well-defined transmembrane protein pores capable of conducting ions selectively or large enough to allow passage of small-molecule fluorophores remains an outstanding challenge^{11,12}. Here, we report the computational design of protein pores formed by two concentric rings of α -helices that are stable and mono-disperse in both water-soluble and transmembrane forms. Crystal structures of the water-soluble forms of a 12 helical and a 16 helical pore are close to the computational design models. Patch-clamp electrophysiology experiments show that the transmembrane form of the 12-helix pore expressed in insect cells allows passage of ions across the membrane with high selectivity for potassium over sodium, which is blocked by specific chemical modification at the pore entrance. The transmembrane form of the 16-helix pore, but not the 12-helix pore, allows passage of biotinylated Alexa Fluor 488 when incorporated into liposomes using *in vitro* protein synthesis. A cryo-EM structure of the 16-helix transmembrane pore closely matches the design model. The ability to produce structurally and functionally well-defined transmembrane pores opens the door to the creation of designer pores for a wide variety of applications.

Recent work on *de novo* membrane protein design has focused on compact bundles of helices without large central cavities^{7,8}. *De novo* design of transmembrane proteins with large pores presents a more stringent thermodynamic challenge, as there is a larger surface area to volume ratio and hence a lower density of stabilizing interactions. As in many natural protein pores, a homo-oligomeric architecture in which a cyclic arrangement of multiple identical copies of a single subunit surrounds the pore is attractive for design as the subunit need not be a large protein. Soluble single-ring coiled-coil assemblies of peptide helices have been designed that surround central pores¹³, but the transformation of soluble oligomeric protein pores into their membrane counterparts is challenging because of the altered thermodynamics of folding in the membrane and possible undesired interactions between non-polar residues introduced to interact with lipids and those at intersubunit interfaces. For example, the oligomerization state of coiled-coil assemblies has been shown to be very sensitive to the placement of nonpolar residues¹⁴, and hence nonpolar residues incorporated to interact with the bilayer could substantially alter oligomeric state.

We set out to design transmembrane protein pores using a two-step approach. We reasoned that protein pores formed from two concentric rings of α -helices containing buried hydrogen bond networks for structural specificity could be stable in both soluble and, after resurfacing the lipid exposed residues with membrane-compatible hydrophobic residues, transmembrane forms. The increased interhelical interaction surfaces in such two-ring bundles could provide greater stability than single-ring structures, particularly for larger pore sizes, and could act together with buried hydrogen bond networks to yield greater structural robustness to conversion between soluble and transmembrane forms. We then sought to design cylindrical two-ring bundles consisting of a minimum of 12 closely packed helices that are assembled

from 2–4 helix monomers, to avoid having to build such large structures from a single polypeptide.

Designing an Ion Channel

We explored the design of water-soluble pores containing helical bundles with a two-ring 6-fold symmetric topology formed from monomeric subunits composed of an inner and outer helix bridged with a short loop. Backbones were generated by sampling α -helical and superhelical parameters of the assemblies using a generalization of the Crick coiled-coil parameterization^{15–17} (see Supplementary Information). After backbone generation and loop closure, we searched for hydrogen-bond networks across intermolecular interfaces using Rosetta HBN¹⁸ and carried out combinatorial sequence optimization for the remaining residue positions keeping the polar networks found by HBN fixed. The interfacial core residues and backbone parameters of the inner helices were set to those of a previously characterized “single-ring” helical bundle¹³ to reduce the design space. Rosetta “fold-and-dock”¹⁹ structure prediction calculations were used to investigate the extent to which the designed sequences encode the design target topologies. Designs for which the lowest energy sampled structures were close to the target design structures (Extended Data Fig. 1a) were selected for experimental characterization.

We obtained synthetic genes encoding the selected designs and expressed them in *Escherichia coli* (*E. coli*). All 3 hexameric designs selected for experimental validation were well expressed and soluble in *E. coli* and purified efficiently by nickel-affinity chromatography and size-exclusion chromatography (SEC). One of the designs was found to form a single homogeneous species with the target oligomeric state using multiangle light scattering (MALS, Extended Data Fig. 2a) and analytical ultracentrifugation (AUC, Extended Data Fig. 1c). The circular dichroism (CD) spectrum of this hexameric design (WSHC6, water-soluble hairpin C6) was highly helical and stable to thermal denaturation up to 95°C (Extended Data Fig. 1b). The small-angle X-ray scattering (SAXS) profile of WSHC6 was close to that computed from the design model, suggesting that WSHC6 folds into the desired shape in solution (Extended Data Fig. 1d). We determined the crystal structure of WSHC6 and found it to be close to the computational design model (Fig. 1a) with a C- α RMSD of 0.89 Å. A chain of discrete water molecules occupies the WSHC6 channel (Fig. 1b, Extended Data Fig. 1e); the narrowest constriction is at Leu51 with a diameter of approximately 4 Å as calculated by HOLE²⁰.

We next sought to convert the stable and structurally well-defined WSHC6 pore into a transmembrane hexameric pore (TMHC6, transmembrane hairpin C6). We redesigned the lipid exposed residues (see Supplementary Information) and incorporated one ring of six glutamate residues (E-ring) and two rings of lysine residues (K-rings) at the openings of the central channel on the extracellular and intracellular side, respectively, to create a polar niche within the pore (Fig. 1c, Extended Data Fig. 3a–b). Similar rings are observed in the calcium channel Orai^{21,22}. The narrowest regions of the TMHC6 pore in the design model are the E-ring (3.3 Å), the K-rings (4.3 Å and 5.7 Å), and two intervening rings of hydrophobic leucine residues (L-rings, 3.6 Å and 4.3 Å) (Fig. 1c). A synthetic gene was obtained for TMHC6 and the protein was expressed in *E. coli*, extracted from the membrane

fraction with detergent, and purified by affinity chromatography and SEC (Extended Data Fig. 2c). TMHC6 eluted as a single peak upon SEC, and CD measurements showed that the design is α -helical and highly thermal stable with a CD spectrum at 95 °C similar to that at 25 °C (Fig. 1d). The protein sedimented as a hexamer in detergent solution in AUC experiments, consistent with the design model (Fig. 1e). Electron microscopy of negatively stained samples showed populations of particles with shape and size consistent with the design model (Extended Data Fig. 3c).

To investigate ion conductance by TMHC6, we performed whole-cell patch-clamp experiments on *Trichoplusia ni* insect cells (Hi5) expressing the designed transmembrane proteins. Using extracellular (bath) and intracellular (electrode) solutions containing 100 mM NaCl and 100 mM NaF, respectively, the TMHC6 construct exhibited a symmetric current/voltage relationship for inward and outward Na⁺ current as a function of membrane potential (Fig. 1f). Gadolinium ion (Gd³⁺), a potent blocker of cation channels, blocked TMHC6 from the extracellular side, reducing the ion conductance to nearly the control value for untransfected cells (Fig. 1f). To test the ion selectivity, Hi5 cells expressing TMHC6 were bathed in a solution containing 100 mM of the chloride salt of the monovalent cations K⁺, Na⁺, Cs⁺, and CH₃NH₃⁺. TMHC6 showed a significantly higher conductance for K⁺, with a current density of 600 pA/pF at +100 mV. The selectivity order was K⁺ (600 pA/pF) \gg CH₃NH₃⁺ = Cs⁺ (170 pA/pF) $>$ Na⁺ (60 pA/pF) \approx Ba²⁺ (54 pA/pF) (Fig. 1g). By comparison, a previously designed transmembrane protein (TMHC2) without a pore⁸ yielded current density for K⁺ of \sim 40 pA/pF at +100 mV, which was close to the background (Extended Data Fig. 3d).

In the design model, the extracellular ring of six Glu44 residues is the site of cation entry (Fig. 2a); we tested this hypothesis by site-directed mutagenesis and chemical modification. Mutation of Glu44 to Phe (E44F) removed the negative charge at the extracellular entry to the pore and reduced the conductance to 308 \pm 81 pA/pF, 51.3 % of the control (Extended Data Fig. 3d). This reduction likely is a direct effect on ion traversal through the pore: the E44F mutant is expressed at a similar level as the TMHC6 parent (Extended Data Fig. 3f), and the purified protein has a similar solution behavior as TMHC6 (Extended Data Fig. 2c). To further test the importance of this site, we constructed the mutant E44H, which deletes the negative charge in this position and adds a partial positive charge. The divalent cation Cd²⁺ blocks the conductance of TMHC6, and 3-fold higher Cd²⁺ concentrations were required to block the E44H mutant, likely because of the reduced electrostatic attraction and/or disrupted metal coordination (Fig. 2b). To enable a chemical biology approach, we constructed the mutant E44C, which removes the negative charge at the extracellular entry to the pore and reduced the conductance to 360 \pm 36 pA/pF, 60% of the control. The chemical reactivity of the substituted Cys residue allowed us to test sulfhydryl reagents as pore blockers. We found that perfusion of negatively charged MTSES, positively charged MTSET, and hydrophobic MTS-TBAE all completely blocked the ion conductance of the TMHC6 E44C mutant within a few minutes under voltage clamp control (Fig. 2c, 2d). The lack of dependence on charge or hydrophilicity suggests that these compounds function by directly sterically blocking the pore. The blockage by these reagents is entirely dependent on the introduced cysteine residue; they had no effect on the original TMHC6 design lacking the cysteine (Fig. 2c, 2d). To determine whether covalent modification had any global effect

on the folding or assembly of the pore, we expressed and purified the TMHC6 E44C mutant from *E. coli* and incubated it with MTSES. Covalent modification was observed by mass spectrometry (Extended Data Fig. 3e), but there was no change in pore assembly or solution behavior more generally (Extended Data Fig. 2d), further suggesting that chemical modification blocks ion conductance by direct steric occlusion.

Taken together, the high ion selectivity, specific inhibition by multivalent cations, and complete block by MTS reagents acting at the extracellular entry to the pore strongly suggest that ion passage is through the designed central transmembrane pore. Leak conductances would not be expected to have these properties. Like some naturally occurring channels, such as the physiologically important store-operated calcium channel Orai²³, single channel recordings on TMHC6 did not yield clear signals. The single channel conductance may be too low, perhaps because of the central non-polar lined portion of the pore.

Why is TMHC6 selective for K⁺? The residue composition and structure of the conductive channel of TMHC6 design are reminiscent of calcium-selective Orai channels, but the selectivity filter(s) of Orai may be too large to selectively conduct dehydrated potassium ions. The TMHC6 pore diameter of 3.3 Å is more tuned for the conductance of partially dehydrated K⁺, as in natural potassium channels, in which K⁺ interacts directly with backbone carbonyls lining the pore without intervening equatorial waters of hydration²⁴. In contrast, voltage-gated sodium and calcium channels, which conduct hydrated Na⁺ and Ca²⁺^{25,26} have pores that are 4.6 Å in diameter, well designed for hydrated sodium and calcium ions^{25–27} but not for K⁺. The ability to design transmembrane pores *de novo* lays the foundation for broad exploration of the pore diameters and chemical interactions that are required for selective conductance of a wide range of ions. This understanding should enable the design of channels which directly modulate cell function. As a first step in this direction, we expressed TMHC6 in a yeast strain that requires potassium for growth, and we found that TMHC6 considerably boosted the growth rate in a K⁺ dependent fashion (Extended Data Fig. 4).

Building a Larger Transmembrane Nanopore

To explore the generation of larger transmembrane pores capable of transporting organic molecules larger than single ions, we designed water-soluble helical bundles with 8-fold symmetry using an approach similar to that described above for WSHC6 except that a starting “single-ring” template was not employed; instead, the structure and sequence of the inner ring of helices was sampled *de novo* in parallel with those of the outer ring. We obtained synthetic genes encoding selected octameric pore designs and expressed them in *E. coli*. Four of five of the octameric designs were well expressed and soluble in *E. coli*, and they could be purified by nickel-affinity chromatography and SEC. However, none of the designs populated only the target octameric state. There are only small differences in interface geometry between C7, C8 and C9 assemblies (the angles between subunits are 51°, 45° and 40°, respectively), and mixtures were observed for most of the designs. We reasoned that achieving a well-defined C8 state would require more precise interface definition; therefore, we carried out a second round of C8 designs with larger intersubunit interaction

surface areas (Extended Data Fig. 5a–b) and more hydrogen bond networks across the interface. Ten of 15 of the second-round designs were expressed and soluble in *E. coli*, and two were found to be mono-disperse and octameric by MALS (Extended Data Fig. 2b). One of the two was further confirmed by AUC (Extended Data Fig. 1h). The CD spectrum of the AUC-verified octameric design (WSHC8, water-soluble hairpin C8) was highly helical with a melting temperature of 85°C (Extended Data Fig. 1g). There was again excellent agreement of the experimental and calculated SAXS profiles indicating that WSHC8 folds into the desired shape in solution (Extended Data Fig. 1i).

We determined the crystal structure for WSHC8 (Fig. 3a–b) and found that the C- α RMSD values between the crystal structure and the design model for the monomeric subunit and the full octameric pore were 0.97 Å and 2.51 Å, respectively. The larger deviation compared to WSHC6 is caused by the slight tilting of the hairpin monomers along the superhelical axis of the complex (Extended Data Fig. 1j). As in the design model, the structure contains a long and continuous central channel with an inner diameter of approximately 10 Å as calculated by HOLE. We converted WSHC8 into an octameric membrane-spanning pore (TMHC8) by redesigning the membrane exposed and pore facing residues of the crystal structure (see Supplementary Information, Extended Data Fig. 5c–d). The design model has a central pore with a diameter of 10 Å and a transmembrane span of 31 Å. A gene encoding TMHC8 was synthesized, the protein expressed in *E. coli*, and the membrane fraction purified and solubilized in detergent. Following affinity chromatography, the protein eluted as a monodisperse peak on SEC (Extended Data Fig. 2e). CD measurements showed that TMHC8 had the expected α -helical secondary structure with a melting temperature of 75°C (Extended Data Fig. 5e). AUC experiments showed that TMHC8 formed complexes with a molecular weight (MW) of 98.9 kDa, which lies in between the MWs of a 14-helix heptamer and a 16-helix octamer (Extended Data Fig. 5g). To resolve this ambiguity, we linked two monomers of TMHC8 together using a short loop to create a four-helix subunit. This redesign, TMH4C4 (Fig. 3d), was purified to homogeneity using nickel-affinity chromatography and SEC (Extended Data Fig. 2f). CD spectroscopy showed that TMH4C4 was fully α -helical and thermally stable up to 95°C (Extended Data Fig. 5f). AUC experiments showed that TMH4C4 sedimented as a tetramer in detergent solution consistent with the 16-helix design model (Extended Data Fig. 5h).

Expression of the designed larger transmembrane nanopore in insect cells resulted in cell death, probably because of induced cell permeability, and hence we were unable to assess the channel activity in these cells. Instead, we used a liposome-based assay coupled to *in vitro* protein synthesis^{28–30}. TMHC6 and TMH4C4 were produced inside liposomes containing streptavidin, and biotinylated Alexa Fluor 488 (MW ~1 kDa) was added outside (Fig. 3e). *In vitro* synthesized TMHC6 and TMH4C4 had similar elution volumes as the bacterially expressed and purified proteins when analyzed by SEC (Extended Data Fig. 6a). Consistent with the much larger pore radius of TMH4C4 compared to TMHC6, we observed considerably more accumulation of dye within proteoliposomes containing TMH4C4 than in proteoliposomes containing an equal ratio of TMHC6, or empty liposomes (Fig. 3f, Extended Data Fig. 6b,c,e). The narrowest dimension of the head group of the fluorophore is approximately 12 Å (Extended Data Fig. 6d), while the nominal diameter of the constriction region of the TMH4C4 pore is estimated to be 10 Å by HOLE, thermal fluctuations of the

side chains and backbone likely allow for permeation by the fluorophore. In contrast, the 3.3 Å constriction of TMHC6 is far too narrow to allow fluorophore passage. Increasing the size of the fluorescent conjugate to 4.6 kDa by inserting poly adenine oligo DNA (A11) between Alexa Fluor 488 and biotin blocked passage through both the TMHC6 or TMH4C4 pores (Fig. 3g), consistent with the estimated hydrodynamic diameter of this compound of 30 Å³¹.

Seeking to obtain an overall structure of the 16-helix transmembrane channel, we used cryogenic electron microscopy (cryo-EM) to determine the three-dimensional (3D) structure of TMH4C4. The protein was concentrated to ~6 mg/ml, applied to EM grids, and cryo-EM images collected and processed following standard protocols (Extended Data Fig. 7a–e). To avoid potential bias, C1 symmetry was applied for automatic image processing and classification, which yielded a dominant 16-helix form containing ~40% of all the 3D classified particles, with the most continuous and intact map among all classes. Further classification and refinement focused on this set of particles resulted in a 5.9 Å resolution map from 64,739 (out of a total of 1,559,110 for 3D classification) selected particles (Fig. 4a, Extended Data Fig. 7d–e). The cryo-EM structure clearly shows the formation of a 16-helix assembly with a large central pore, consistent with the design model built from the crystal structure of the soluble form (Fig. 4a). Density encircling the membrane-spanning region likely originates from surrounding detergent molecules (Extended Data Fig. 7e–f). A structure model of TMH4C4 built based on the EM map (Fig. 4a–b) had some deviation among the four protomers so the tetramer is not perfectly symmetric (Fig. 4c), but the central pore-containing 16-helix structure corresponding to the original TMH4C4 design is clearly resolved, and aligns well to the design model (Fig. 4b).

Conclusion

Our advances in designing structurally well defined transmembrane pores (for comparison to previous *de novo* membrane protein designs, see Extended Data Fig. 8), like advances in protein design generally^{8,10,32}, both inform our understanding of general principles of protein biophysics, and open the door for a wide range of applications. From the membrane protein folding perspective, our success in designing transmembrane homo-oligomeric structures with hydrogen bond network containing subunit interfaces suggests that the combination of the substantial buried surface area and polarity of the interaction surfaces makes them robust to changes in the surrounding environment and reduces confounding effects resulting from the interactions with the purely hydrophobic lipid facing residues during folding. This approach allows the construction of quite substantial pores with environments very different from that of the surrounding lipids: the TMHC6 pore clearly shows selective transmembrane ion conductance, and the 10 Å diameter TMH4C4 pore clearly evident in the cryo-EM structure is lined with polar residues and provides passage to solutes as large as biotinylated Alexa Fluor 488.

Our strategy of first designing soluble pore-containing structures, and then converting the stable designs into transmembrane proteins following crystal structure determination, leverages the considerably more straightforward structural characterization of soluble proteins as a key step toward building complex transmembrane proteins with a high success rate (see the Supplementary Information). Building on the channels described in this paper,

custom design now provides a platform to understanding the underlying chemistry and physics of solute permeation and selectivity by modulating pore structures and selectivity filters in ways that are not possible with native channels, and also enables a wide range of applications. For example, in nanotechnology, custom designed pores could provide new routes to generating membranes with selective permeabilities, sensing molecules in the environment, and controlling cellular behaviour.

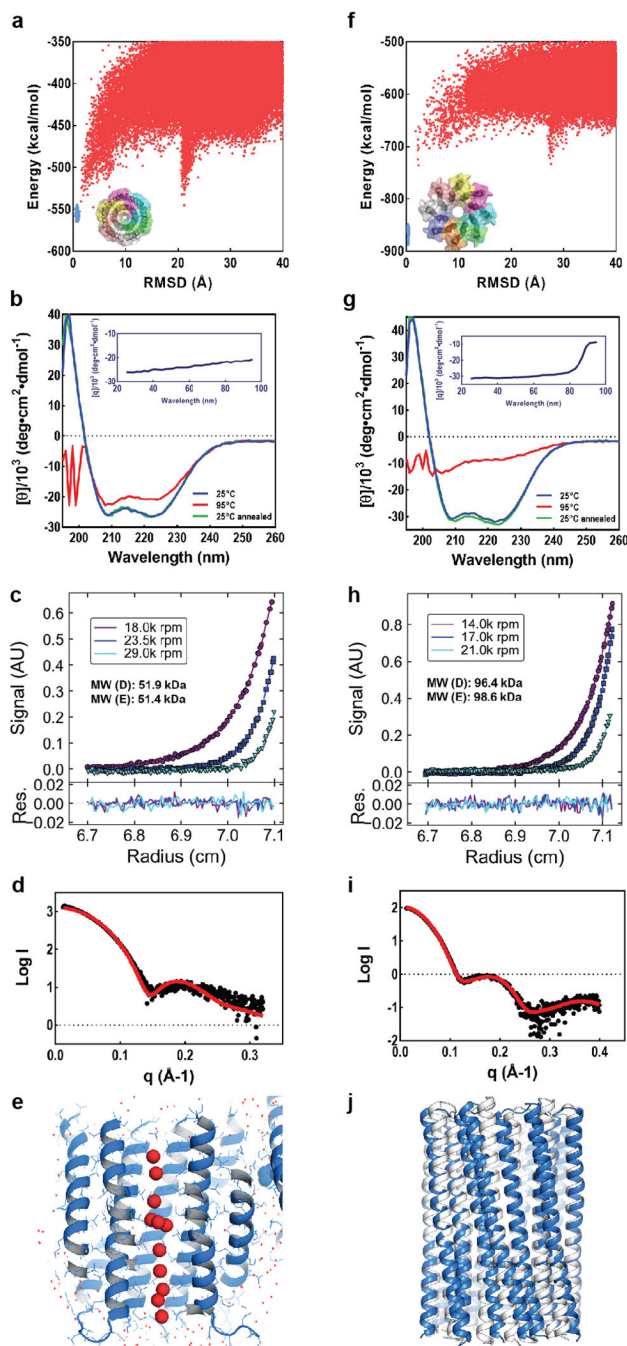
Code availability

All program code is in Rosetta distribution (<https://www.rosettacommons.org>). Example design protocols are provided in the Supplementary Information.

Data availability

Coordinates and structure files have been deposited to the Protein Data Bank with accession codes 6TJ1 (WSHC6, P2₁22₁), 6TMS (WSHC6, P1), and 6O35 (WSHC8). An EM map of TMH4C4 and the associated structure model have been deposited in the Electron Microscopy Data Bank and Protein Data Bank with the following accession codes: EMD-30126 and PDB 6M6Z.

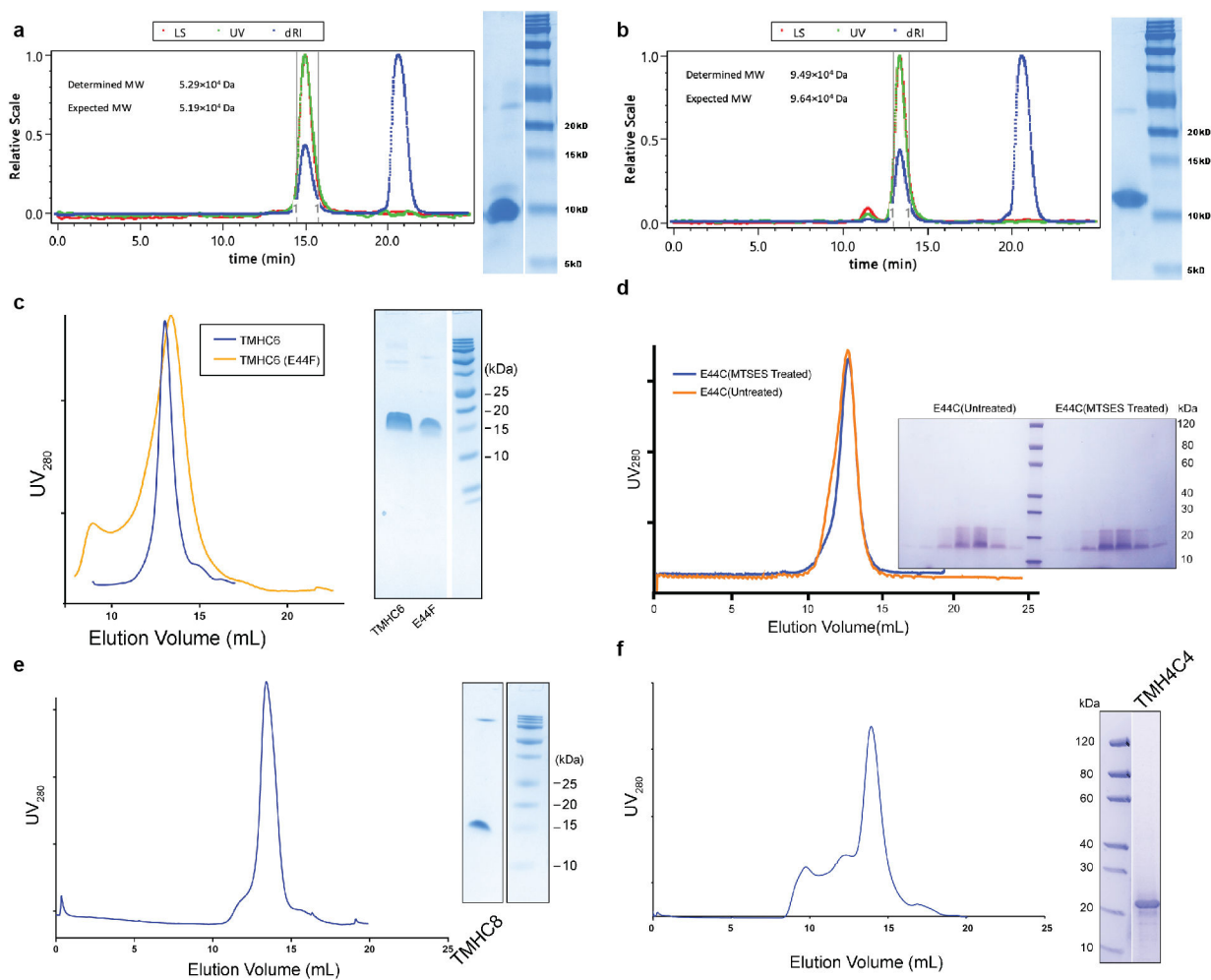
Extended Data



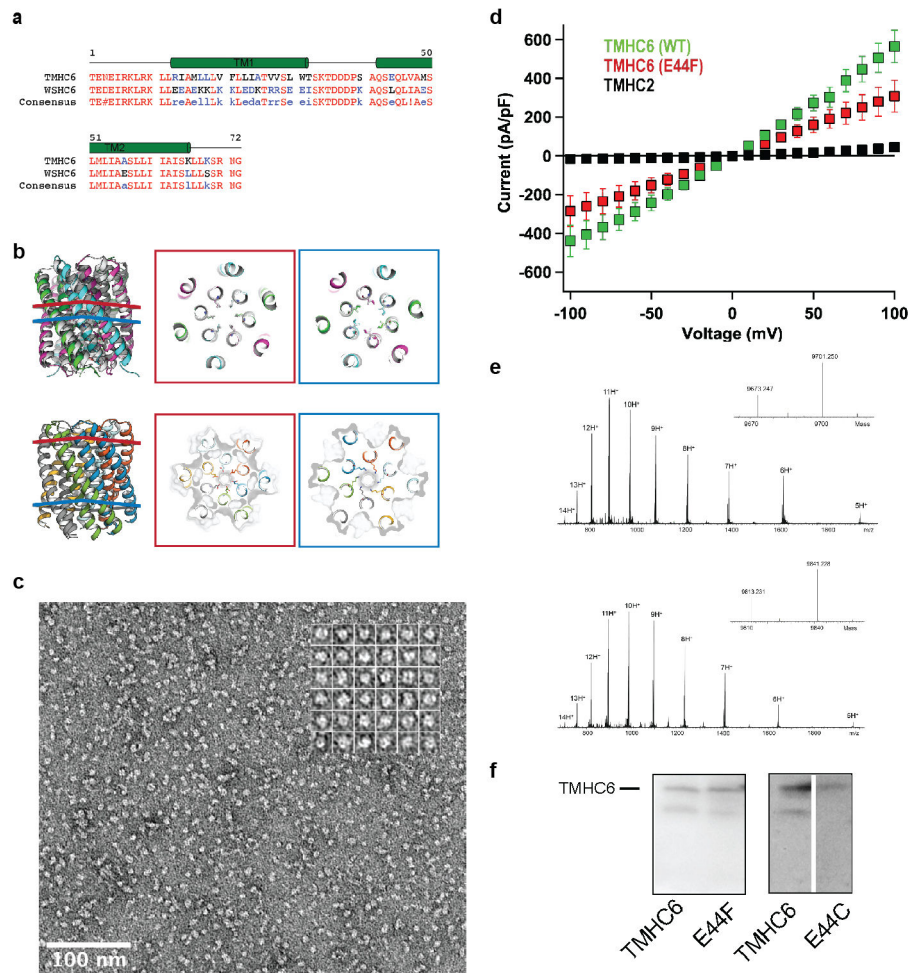
Extended Data Fig. 1 | Design and characterization of water-soluble pores.

(a & f) Design models (insets) and energy versus RMSD plots generated from Rosetta “fold-and-dock” structure prediction calculations. The predicted structures converge on the design models with RMSD values less than 2.0 Å. Structures in the alternative energy minima at large RMSD positions also recapitulate the design models but with chain identities in the RMSD calculations reversed. (b & g) Wavelength-scan and temperature-scan (insets) CD spectra. WSHC6 does not melt up to 95°C, while WSHC8 has a melting temperature of

85°C. The overlap of the pre- and post-annealing CD spectra indicates that the thermal denaturation is reversible. (c & h) Representative analytical ultracentrifugation sedimentation-equilibrium curves at three different rotor speeds for WSHC6 and WSHC8, 0.2 OD₂₃₀ and 0.3 OD₂₃₀ in PBS (pH 7.4), respectively. The determined oligomeric states match those of the design models. (d & i) Small-angle X-ray Scattering (SAXS) characterization. The experimental scattering profiles (black) are similar to scattering profiles computed from the design models (red). (e) The chain of water molecules in the pore of WSHC6 crystal structure (red spheres) is verified by processing the data and refining the structure in the P1 space group. (j) Overlay of the crystal structure (blue) and the design model (gray) of WSHC8. Helices are more tilted in the crystal structure than in the design model.



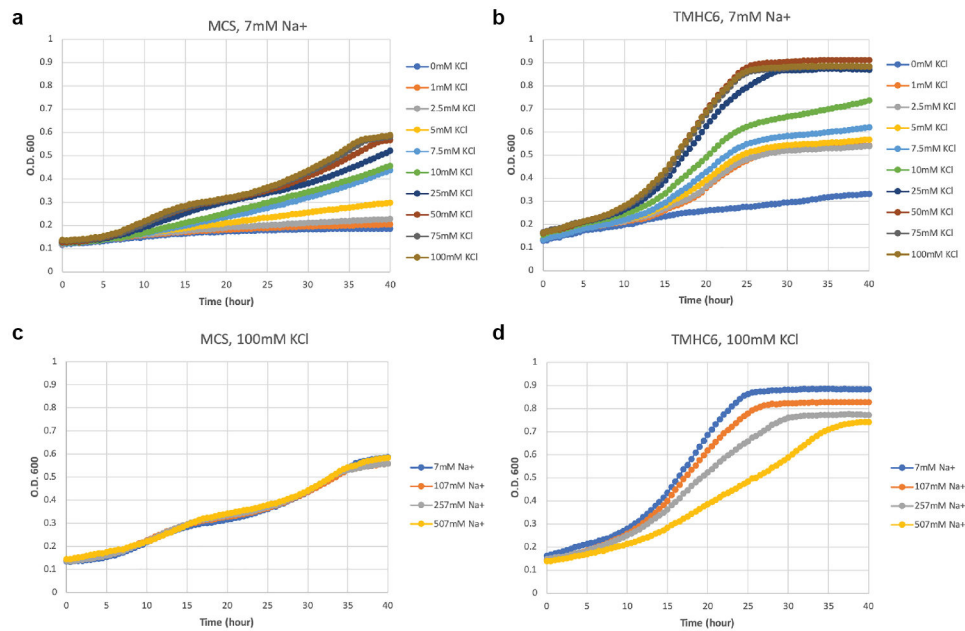
Extended Data Fig. 2 | Representative SEC and SDS-PAGE of the designed proteins. (a & b) WSHC6 and WSHC8. MWs are determined by coupling SEC with MALS. (c) TMHC6 and E44F mutants. (d) TMHC6 E44C mutant treated or untreated with MTSES reagent. (e) TMHC8. (f) TMH4C4. These experiments were repeated twice with similar results.



Extended Data Fig. 3 | Comparisons between WSHC6 and TMHC6 and additional characterizations of TMHC6 and mutants.

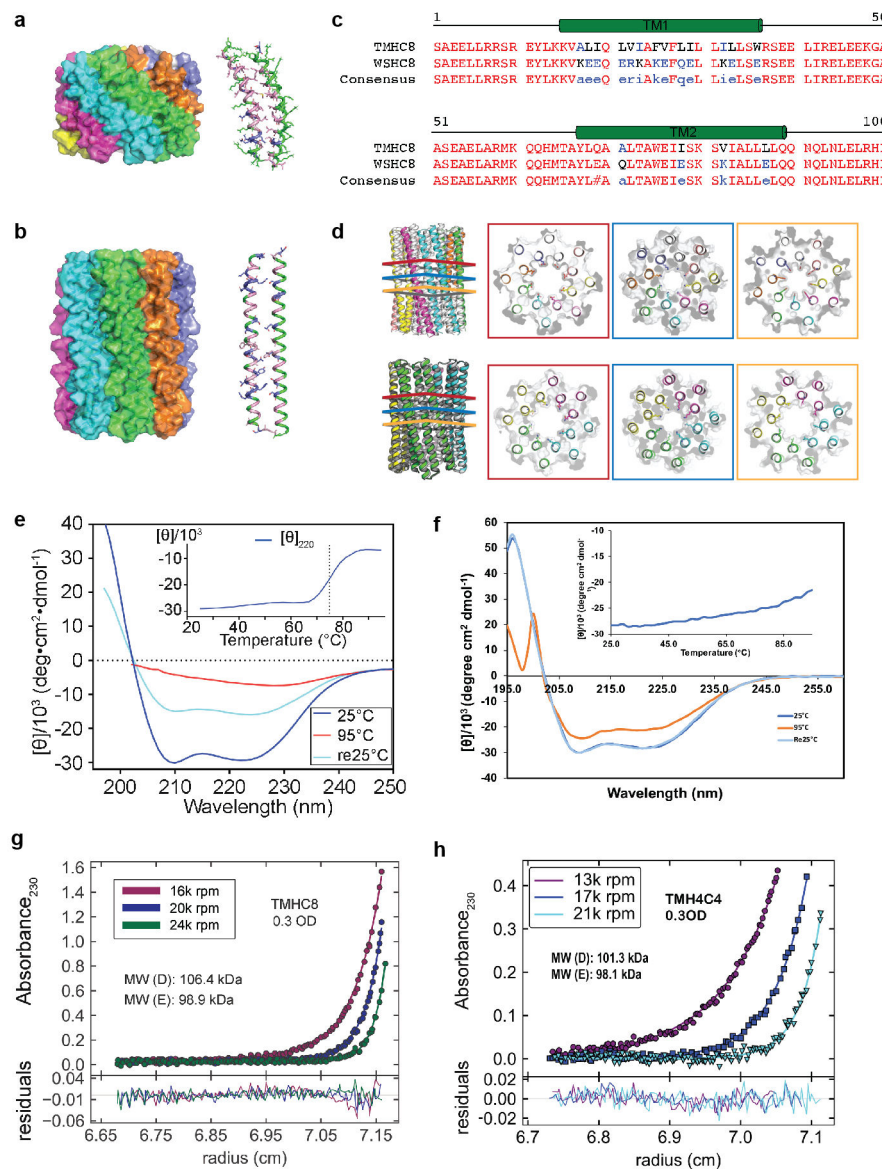
(a) Sequence alignment of TMHC6 with WSHC6. (b) Pore-lining residues in WSHC6 and TMHC6. Top row: overlay of the crystal structure (colors) and the design model (gray) of WSHC6. The pore is lined with alternating leucine (red layer) and isoleucine (blue layer) residues. Bottom row: the TMHC6 pore is lined with E44 ring (red layer) and K65 ring (blue layer) at the extracellular and intracellular sides, respectively. (c) Negative stain EM for TMHC6 in amphipols. Protein particles on the EM grid showed round shape and size consistent with the design model (scale bar at the bottom left, 100 nm). Inset: close-up view of representative particles; each side of the particle frames represent 12.8 nm. (d) Disrupting mutation in the TMHC6 pore entrance reduces the current. The E44F single mutant reduced the K^+ current to half of that for TMHC6. TMHC2, a previously designed transmembrane protein without a pore, does not conduct ions across the membrane. 3 cells were measured for each protein and the mean (data points) and standard error of measurement (s.e.m., error bars) are plotted. (e) The covalent modification of TMHC6 E44C mutant by MTSES. Mass spectrometry results show that there is a 140 Da increase in molecular weight for the mutant after MTSES treatment, in agreement with the predicted value. (f) Expression of TMHC6 and mutants in insect cells for the whole-cell patch-clamp experiments. The same amount of cells were loaded into the gel and the expression levels for two variants were examined by

western blot. The E44F mutant had similar, if not higher, expression level as TMHC6. The E44C mutant expressed at a slightly lower level compared to TMHC6. These experiments were repeated three times with similar results.



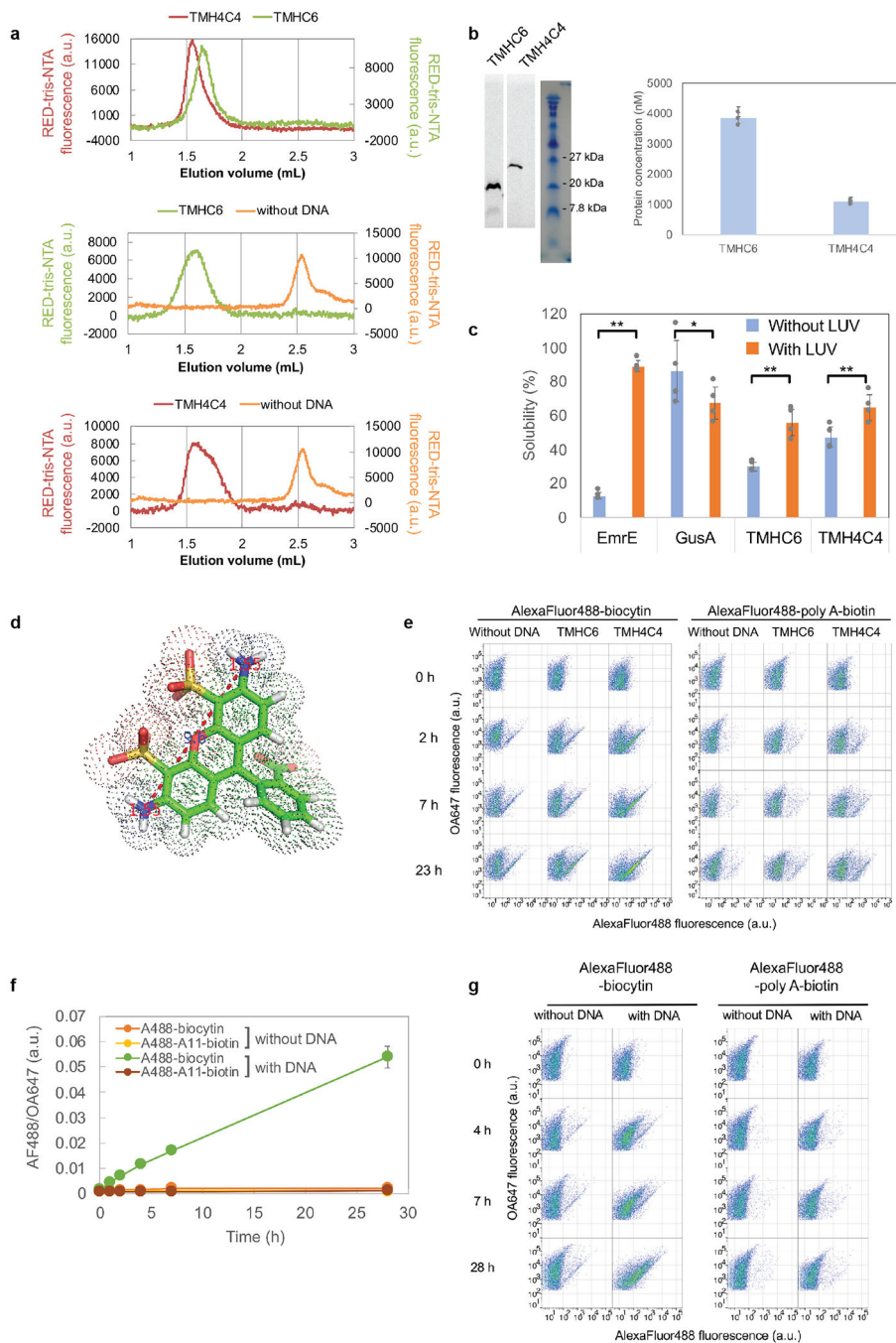
Extended Data Fig. 4 | The expression of TMHC6 complements a yeast strain defective of K⁺ uptake.

(a) SGY1528 with an empty vector MCS grew slowly when K⁺ concentration was lower than 5 mM. Observed growth rate showed dependency on extracellular K⁺ concentration. (b) SGY1528 supplemented with the TMHC6 gene rescued the yeast growth at lower extracellular K⁺ concentrations (1 mM - 5 mM) and showed increased growth rates at higher extracellular K⁺ concentrations (7.5 mM - 100 mM). (c & d) With increasing concentrations of extracellular Na⁺, TMHC6 yeast showed decreased growth rate (d) in comparison with the insensitive growth rates of MCS yeast (c). These results suggest that TMHC6 conducts K⁺ and complements the defective K⁺ uptake in strain SGY1528; this rescuing effect is sensitive to extracellular Na⁺ concentrations indicating an increased Na⁺ permeability. A detailed method section is described in Supplementary Materials. The minimal medium and the seeding process are carefully designed to not contain or bring in potassium. The background K⁺ concentration should be low, which is suggested by the sharp difference between curves for 0 and 1 mM K⁺ in the TMHC6 case.



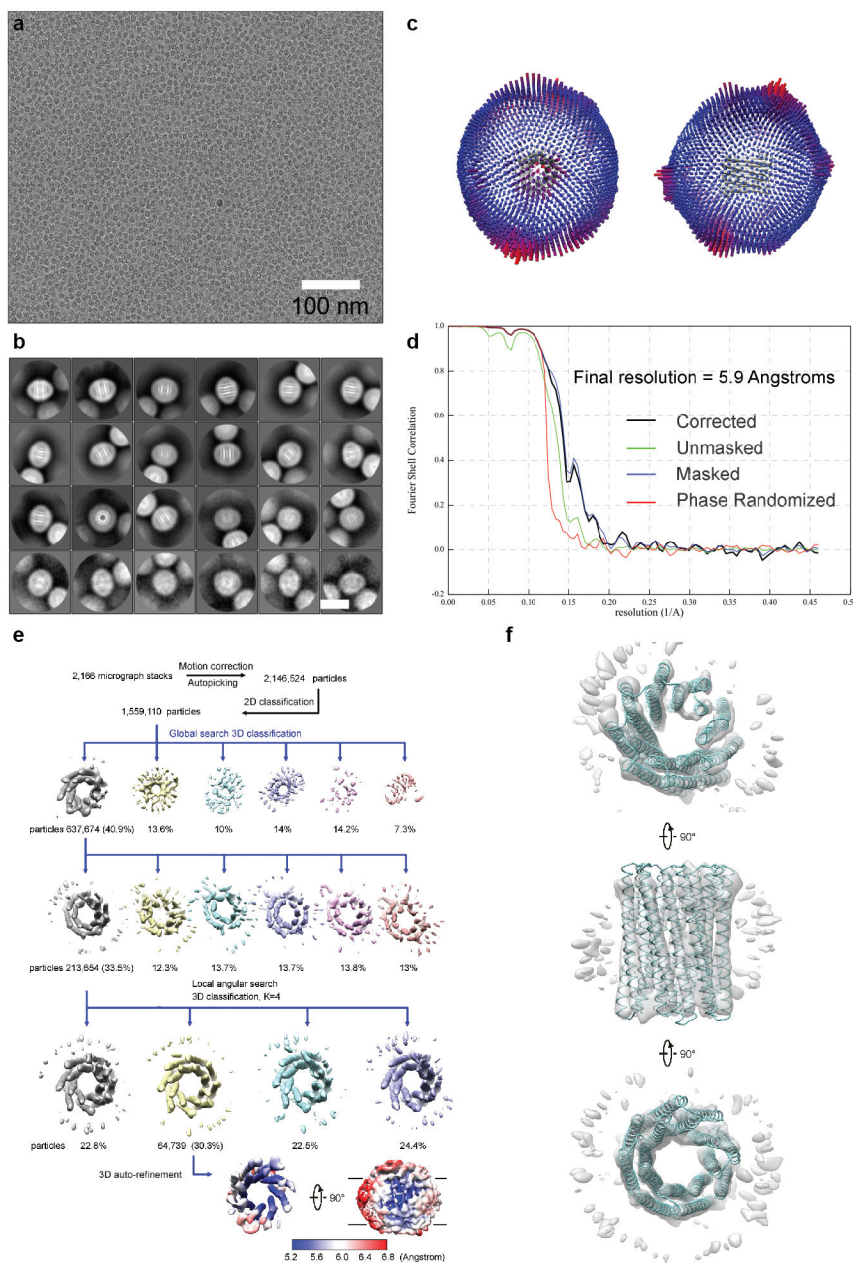
Extended Data Fig. 5 |. Design and additional characterizations of the designed 16-helix pores. (a & b) Design models from the first and second rounds of water-soluble designs. The monomers of the first round designs (a, 70 amino acids) are considerably smaller than those of the second round (b, 100 amino acids). (c) Sequence alignment of TMHC8 with WSHC8. (d) Pore-lining residues in WSHC8 and TMH4C4. The crystal and cryoEM structures are in colors. The design models are in gray. Top row: The lumen of WSHC8 pore is freely water-accessible, so the residues inside the pore are all polar. Shown in the figure are three representative layers of the pore-lining residues in the crystal structure, Glu69 ring (red), Lys80 ring (blue), and Glu87 (orange). The missing heavy atoms of these flexible residues are built using Rosetta with backbone constraints. Bottom row: three pore-lining layers in the cryo-EM structure of TMH4C4 corresponding to the three layers in the top row. Glu69 and Glu87 are replaced with glutamine and leucine, respectively. (e & f) CD spectra and thermal stability of 16-helix transmembrane pores. An unfolding transition is observed at

~75°C for TMHC8 (e). TMH4C4 (f) is thermally stable up until 95°C. (g & h) Representative AUC sedimentation-equilibrium curves of 16-helix transmembrane nanopores. By fitting the data globally as a single ideal species in solution, TMHC8 is shown to form complexes with a MW of 98.9 kDa, which is in between the MWs of a heptamer and an octamer. The MW of TMH4C4 is determined to be 98.1 kDa, very close to the MW of a tetramer. ‘MW (D)’ refers to the molecular weight of the oligomer design and ‘MW (E)’ refers to the molecular weight determined in the experiment.



Extended Data Fig. 6 | *In vitro* protein synthesis and characterizations of TMHC6 and TMH4C4.

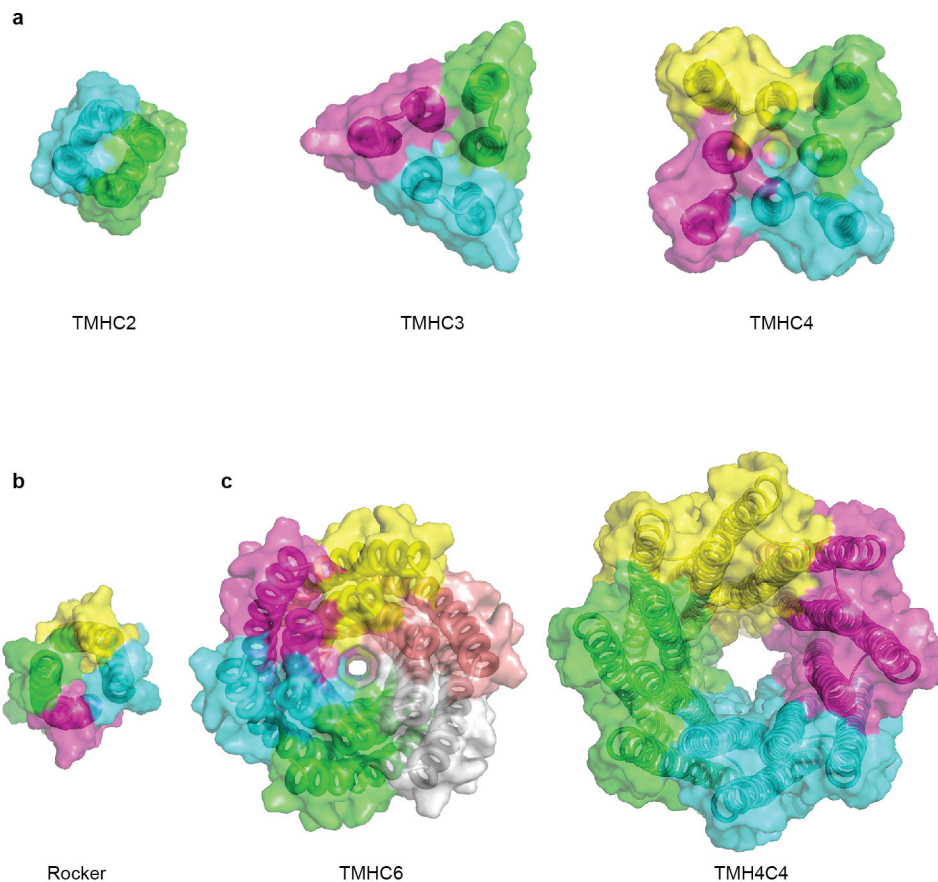
(a) SEC analyses of TMHC6 and TMH4C4 purified from *E. coli* (top) and synthesized *in vitro* (middle and bottom). (b) The *in vitro* synthesized products were analyzed by SDS-PAGE and autoradiography⁵¹. The means of three independent experiments are shown. The error bars indicate s.e.m.. (c) EmrE, one of the *E. coli* derived membrane proteins, showed strong interaction with LUV while GusA, soluble enzyme, did not. For TMHC6 and TMH4C4, fraction interacting with LUV was found to be 25.9% and 17.6%, respectively, among synthesized, indicating that the fraction associated with the membrane is similar between them. The mean of four independent experiments are shown. The error bars indicate s.e.m.. Student's paired t-Test with a two-sided distribution was used to calculate the *p* values (**p*<0.05, ***p*<0.01; from the left to right *p*=1.65×10⁻⁶, 0.0357, 0.0040, 0.0024). (d) The narrowest dimension of the head group of Alexa Fluor 488-biotin is approximately 12 Å. The Van der Waals radius of nitrogen atoms is 1.55 Å. (e) Representative original data for Fig. 3f. Data of approximately 15,000 to 20,000 particles are shown. Similar results were obtained with 7 independent experiments. (f) Flow Cytometry data of the liposomes with pores made of α-hemolysin (AH). Time courses of the median values of the histogram of AF488/OA647 fluorescence, which represents the concentration of the Alexa Fluor 488 inside the liposome are shown. The means of three independent experiments are plotted with the error bars indicating the s.e.m.. (g) Representative original data of (f). Similar results were obtained with 3 independent experiments.



Extended Data Fig. 7 | Cryo-EM resolution estimation and data processing.

(a) Exemplary cryo-EM micrograph of purified TMH4C4 after drift correction and dose-weighting. All the micrographs were with similar results. (b) Class averages after the final round of 2D classification sorted in descending order by the number of particles in each class. The white scale bar in the bottom right panel indicates 10 nm. (c) Angular distribution plot for the final reconstruction from two different views. (d) The gold-standard Fourier shell correlation (FSC) curves for the 3D reconstruction. Deriving map resolution from FSC = 0.143 is indicated. (e) Processing of 2,166 EM micrographs resulted in a total number of 2,146,524 TMH4C4 particles. After a 2D sub-classification, 3D classifications and refinement, a final dataset containing 64,739 particles was used for 3D auto-refinement within Relion 3.0. Local resolution of TMH4C4 was determined within Relion 3.0.

Coloured full views (lower lane) from two different orientations illustrate the resolution of different regions in the protein. The low resolution “belt” in the right panel indicates the density for detergents. (f) EM density from 213,654 particles. An EM map (gray) from the second round of 3D classification from 213,654 particles (e) is shown in three perpendicular views. Superposition of the cryo-EM structure of TMH4C4 (cyan) to the map shows a good fit.



Extended Data Fig. 8 | Advances in membrane protein design: from compact helical bundles to transmembrane pores.

(a-b) Surface view of previously reported *de novo* designed transmembrane proteins^{7,8}. (c) Surface view of designer transmembrane pores described in this study. Central pores with different sizes are visible.

Extended Data Table 1 |

Crystallographic statistics for WSHC6 and WSHC8.

	WSHC6	WSHC6	WSHC8
Data collection			
Space group	P2 ₁ 2 ₂ 1	P1	P2 ₁ 2 ₁ 2
Cell dimensions			
<i>a, b, c</i> (Å)	45.72, 54.13, 79.17	45.88, 54.33, 79.33	59.44, 103.68, 72.98

	WSHC6	WSHC6	WSHC8
a, b, g (°)	90, 90, 90	89.80, 90.08, 89.77	90, 90, 90
Resolution (Å)	45.7–2.35	54.2 – 2.6	34.4 – 2.4 (2.49 – 2.4)
R_{sym} or R_{merge}	0.114 (0.561)	0.145 (0.648)	0.192 (1.698)
$I/\sigma I$	10.7 (1.5), 8.6 (0.7), 9.6 (2.5) [#]	5.0 (1.4), 4.9 (1.0), 7.0 (2.6) [#]	8.3 (1.4)
Completeness (%)	95.3 (95.6)	98.7 (98.7)	99.6 (99.4)
Redundancy	2.8 (2.9)	3.0 (3.0)	7.0 (7.2)
Refinement			
Resolution (Å)	40.0 – 2.4	20 – 2.6	34.4 – 2.4
No. reflections	14091	44867	18183
$R_{\text{work}} / R_{\text{free}}$	0.254/0.288	0.279/0.287	0.261/0.298
No. atoms	1641	7215	2931
Protein	1608	6674	2914
Ligand/ion			
Water	33	541	17
B -factors	67.9	48.0	59.4
Protein	68.3	46.5	59.5
Ligand/ion		41.6	
Water	49.0	57.0	43.8
R.m.s. deviations			
Bond lengths (Å)	0.004	0.095	0.002
Bond angles (°)	0.86	2.57	0.37

* Data for WSHC6 and WSHC8 structures were collected from a single crystal. Values in parentheses are for the highest-resolution shell.

[#] $I/\sigma(I)$ (along a*, b* and c* axes)

Extended Data Table 2 |

Cryo-EM Image Processing Statistics for TMH4C4.

	TMH4C4 (EMD-30126) (PDB-6M6Z)
Data collection and processing	
EM equipment	Titan Krios (Thermo Fisher Scientific)
Magnification	81,000
Voltage (kV)	300 kV
Detector	Gatan K3 Summit
Energy Filter	Gatan GIF Quantum, 20 eV slit
Electron exposure (e ⁻ /Å ²)	50
Defocus range (µm)	-1.2 ~ -2.2
Pixel size (Å)	1.087
Initial particle images (no.)	2,146,524
Final particle images (no.)	64,739
Symmetry imposed	C1
Map resolution (Å)	5.9

TMH4C4 (EMD-30126) (PDB-6M6Z)	
FSC threshold	0.143
Map resolution range (Å)	5.2 – 7.2
Refinement	
Initial model used (PDB code)	n/a (<i>de novo</i>)
Model resolution (Å)	7.7
FSC threshold	0.5
Map sharpening <i>B</i> factor (Å ²)	–292
Model composition	
Non-hydrogen atoms	6600
Protein residues	804
Ligands	n/a
R.m.s. deviations	
Bond lengths (Å)	0.016
Bond angles (°)	1.3
B factors (Å²)	
Protein	169.4
Ligand	n/a
Validation	
MolProbity score	0.52
Clashscore	0.05
Poor rotamers (%)	0
Ramachandran plot	
Favored (%)	99.63
Allowed (%)	100
Disallowed (%)	0

Supplementary Material

Refer to Web version on PubMed Central for supplementary material.

Acknowledgments

We thank A. Kang for assistance with crystallization, Banu Sankaran of the Berkeley Center for Structural Biology at the Advanced Light Source for help with X-ray diffraction data collection, J. Sumida for AUC support, L. Carter for assistance with SEC-MALS, U. Nattermann, Q. Zhou and H. Shen for assistance with EM, SIBYLS mail-in SAXS program at the Advanced Light Source (ALS) for SAXS data collection, L. Jan, T. Cheng and R. Zhou from UCSF for sharing yeast strain SGY1528, and Rosetta@Home volunteers for contributing computing resources. The cryo-EM work was performed at the Cryo-EM Facility of Westlake University. We thank the Arnold and Mabel Beckman Cryo-EM Center at the University of Washington for access to electron microscopes. We thank the Information Technology Center of Westlake University for providing computation support. We thank the Mass Spectrometry & Metabolomics Core Facility of Westlake University for mass-spectrometry analysis. This work was supported by the Howard Hughes Medical Institute, the Air Force Office of Scientific Research (FA9550-18-1-0297), and NSF grant CHE 1629214. P. Lu was supported by NSFC Project 31901054, Tencent Foundation, and the foundation of Westlake University. SAXS data collection at SIBYLS is funded through DOE BER Integrated Diffraction Analysis Technologies (IDAT) program and NIGMS grant P30 GM124169-01, ALS-ENABLE. T.M. was in part supported by KAKENHI grants 17H00888 from JSPS. BFL and XYP are supported by a Wellcome Trust Investigator award (200873/Z/16/Z). The ALS-ENABLE beamlines are supported in part by the

National Institutes of Health, National Institute of General Medical Sciences, grant P30 GM124169-01 and the Howard Hughes Medical Institute. The Advanced Light Source is a Department of Energy Office of Science User Facility under Contract No. DE-AC02-05CH11231.

References

1. Gilbert RJC, Bayley H & Anderluh G Membrane pores: from structure and assembly, to medicine and technology. *Philos. Trans. R. Soc. Lond. B Biol. Sci* 372, (2017).
2. Eisenstein M An ace in the hole for DNA sequencing. *Nature* 550, 285–288 (2017). [PubMed: 29022596]
3. Kasianowicz JJ, Brandin E, Branton D & Deamer DW Characterization of individual polynucleotide molecules using a membrane channel. *Proc. Natl. Acad. Sci. U. S. A* 93, 13770–13773 (1996). [PubMed: 8943010]
4. Clarke J et al. Continuous base identification for single-molecule nanopore DNA sequencing. *Nat. Nanotechnol* 4, 265–270 (2009). [PubMed: 19350039]
5. Lear JD, Wasserman ZR & DeGrado WF Synthetic amphiphilic peptide models for protein ion channels. *Science* 240, 1177–1181 (1988). [PubMed: 2453923]
6. Akerfeldt KS, Lear JD, Wasserman ZR, Chung LA & DeGrado WF Synthetic peptides as models for ion channel proteins. *Acc. Chem. Res* 26, 191–197 (1993).
7. Joh NH et al. De novo design of a transmembrane Zn²⁺-transporting four-helix bundle. *Science* 346, 1520–1524 (2014). [PubMed: 25525248]
8. Lu PL et al. Accurate computational design of multipass transmembrane proteins. *Science* 359, 1042–1046 (2018). [PubMed: 29496880]
9. Mahendran KR et al. A monodisperse transmembrane α -helical peptide barrel. *Nat. Chem* 9, 411–419 (2017). [PubMed: 28430192]
10. Mravic M et al. Packing of apolar side chains enables accurate design of highly stable membrane proteins. *Science* 363, 1418–1423 (2019). [PubMed: 30923216]
11. Joh NH, Grigoryan G, Wu Y & DeGrado WF Design of self-assembling transmembrane helical bundles to elucidate principles required for membrane protein folding and ion transport. *Philos. Trans. R. Soc. Lond. B Biol. Sci* 372, (2017).
12. Niitsu A, Heal JW, Fauland K, Thomson AR & Woolfson DN Membrane-spanning α -helical barrels as tractable protein-design targets. *Philos. Trans. R. Soc. Lond. B Biol. Sci* 372, 20160213 (2017). [PubMed: 28630153]
13. Thomson AR et al. Computational design of water-soluble α -helical barrels. *Science* 346, 485–488 (2014). [PubMed: 25342807]
14. Rhys GG et al. Maintaining and breaking symmetry in homomeric coiled-coil assemblies. *Nat. Commun* 9, 4132 (2018). [PubMed: 30297707]
15. Crick FHC The Fourier transform of a coiled-coil. *Acta Crystallogr.* 6, 685–689 (1953).
16. Grigoryan G & DeGrado WF Probing designability via a generalized model of helical bundle geometry. *J. Mol. Biol* 405, 1079–1100 (2011). [PubMed: 20932976]
17. Huang PS et al. High thermodynamic stability of parametrically designed helical bundles. *Science* 346, 481–485 (2014). [PubMed: 25342806]
18. Boyken SE et al. De novo design of protein homo-oligomers with modular hydrogen-bond network-mediated specificity. *Science* 352, 680–687 (2016). [PubMed: 27151862]
19. Das R et al. Simultaneous prediction of protein folding and docking at high resolution. *Proc. Natl. Acad. Sci. U. S. A* 106, 18978–18983 (2009). [PubMed: 19864631]
20. Smart OS, Neduvilil JG, Wang X, Wallace BA & Sansom MSP HOLE: A program for the analysis of the pore dimensions of ion channel structural models. *J. Mol. Graph* 14, 354–360 (1996). [PubMed: 9195488]
21. Hou X, Pedi L, Diver MM & Long SB Crystal structure of the calcium release-activated calcium channel Orai. *Science* 338, 1308–1313 (2012). [PubMed: 23180775]
22. Hou X, Burstein SR & Long SB Structures reveal opening of the store-operated calcium channel Orai. *Elife* 7, (2018).

23. Dynes JL, Amcheslavsky A & Cahalan MD Genetically targeted single-channel optical recording reveals multiple Orai1 gating states and oscillations in calcium influx. *Proc. Natl. Acad. Sci. U. S. A* 113, 440–445 (2016). [PubMed: 26712003]
24. Jiang Y et al. X-ray structure of a voltage-dependent K⁺ channel. *Nature* 423, 33–41 (2003). [PubMed: 12721618]
25. Payandeh J, Scheuer T, Zheng N & Catterall WA The crystal structure of a voltage-gated sodium channel. *Nature* 475, 353–358 (2011). [PubMed: 21743477]
26. Tang L et al. Structural basis for Ca²⁺ selectivity of a voltage-gated calcium channel. *Nature* 505, 56–61 (2014). [PubMed: 24270805]
27. Pan X et al. Structure of the human voltage-gated sodium channel Nav1.4 in complex with β 1. *Science* 362, (2018).
28. Fujii S et al. Liposome display for in vitro selection and evolution of membrane proteins. *Nat. Protoc.* 9, 1578–1591 (2014). [PubMed: 24901741]
29. Fujii S, Matsuura T, Sunami T, Kazuta Y & Yomo T In vitro evolution of α -hemolysin using a liposome display. *Proc. Natl. Acad. Sci. U. S. A* 110, 16796–16801 (2013). [PubMed: 24082135]
30. Dwidar M et al. Programmable Artificial Cells Using Histamine-Responsive Synthetic Riboswitch. *J. Am. Chem. Soc* 141, 11103–11114 (2019). [PubMed: 31241330]
31. Sim AYL, Lipfert J, Herschlag D & Doniach S Salt dependence of the radius of gyration and flexibility of single-stranded DNA in solution probed by small-angle x-ray scattering. *Phys. Rev. E Stat. Nonlin. Soft Matter Phys* 86, 021901 (2012). [PubMed: 23005779]
32. Huang P-S, Boyken SE & Baker D The coming of age of de novo protein design. *Nature* 537, 320–327 (2016). [PubMed: 27629638]
33. Song L et al. Structure of staphylococcal alpha-hemolysin, a heptameric transmembrane pore. *Science* 274, 1859–1866 (1996). [PubMed: 8943190]
34. Pettersen EF et al. UCSF Chimera?A visualization system for exploratory research and analysis. *Journal of Computational Chemistry* vol. 25 1605–1612 (2004). [PubMed: 15264254]

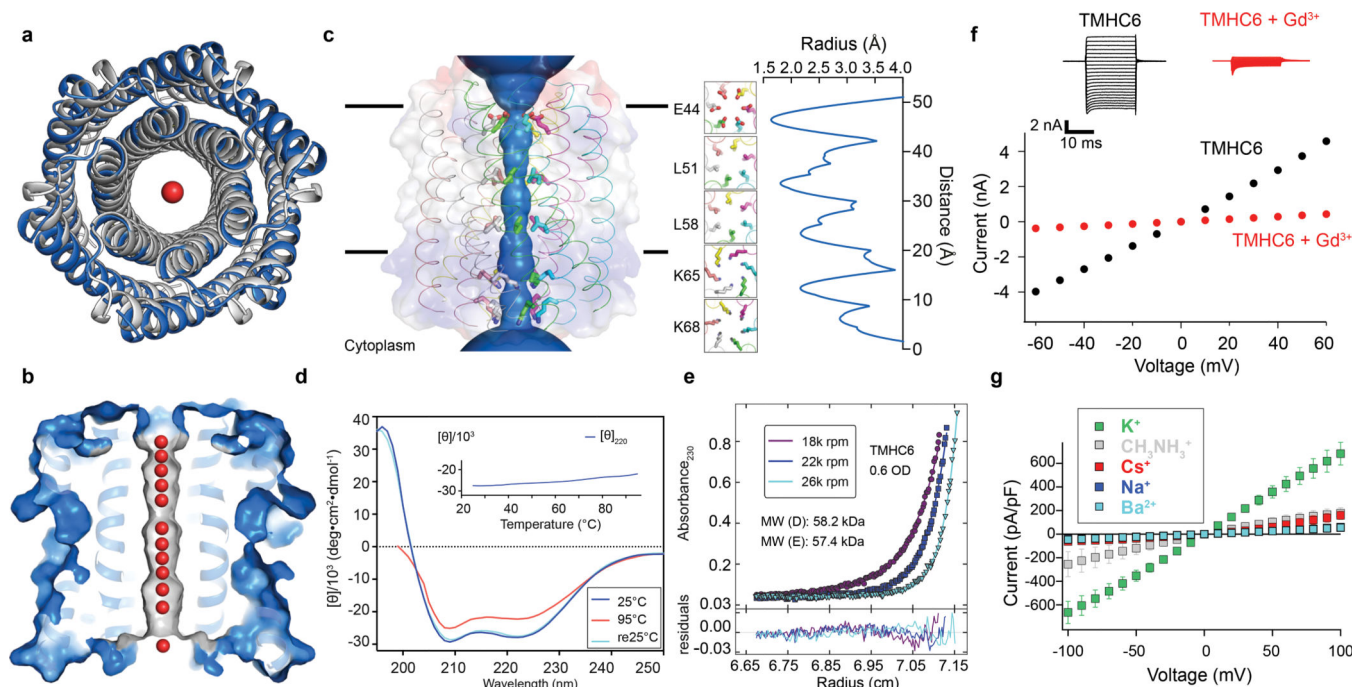


Figure 1. The X-ray crystal structure of the water-soluble hexameric WSHC6 and the ion conductivity of the 12-helix TMHC6 transmembrane channel.

(a) Superposition of backbones of the crystal structure (blue) and the design model (gray) of WSHC6. The C- α RMSD between the crystal structure and the design model is 0.89 Å. (b) The cross section of the WSHC6 channel. A chain of water molecules (red) occupies the central pore (Extended Data Fig. 1e). (c) TMHC6 channel model. The permeation path, calculated by HOLE²⁰, is illustrated by the blue surface in the left panel. Constriction sites along the channel are the E-ring (E44), the K-rings (K65, K68), and two intervening L-rings (L51, L58). Right: the radius of the pore along the permeation path. (d) CD spectra and temperature melt (inset) of the TMHC6 channel. No apparent unfolding transition is observed up to 95°C. Re25°C spectrum is taken when the sample cools back to 25°C after the thermal melt scan. (e) AUC sedimentation-equilibrium curves at three different rotor speeds for TMHC6 yield a measured molecular weight of ~58 kDa consistent with the designed hexamer. “MW (D)” and “MW (E)” indicate the molecular weight of the oligomer design and that calculated from the experiment, respectively. (f) Conductivity in whole-cell patch-clamp experiment on insect cells expressing TMHC6. The channel blocker Gd³⁺ diminished ion conductance to that of untransfected cells. (g) TMHC6 has considerably higher conductance for K⁺ than Na⁺, Cs⁺, CH₃NH₃⁺ and Ba²⁺. 10 cells were measured for each permeant ion species and the mean (data points) and standard error of measurement (s.e.m., error bars) are plotted.

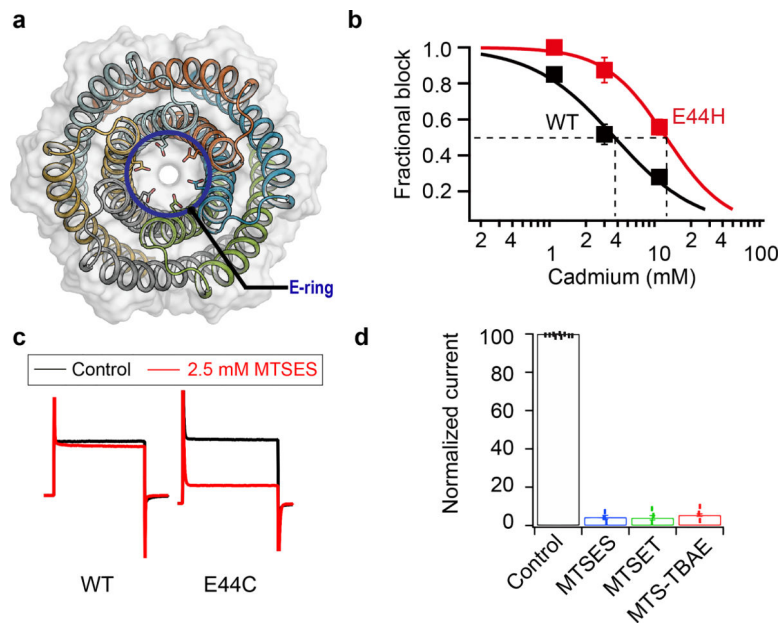


Figure 2. Blocking of the ion conductance of TMHC6 with site-directed mutagenesis and chemical biology.

(a) The extracellular ring of six Glu44 residues (E-ring, shown as sticks) is a likely site for cation entry. (b) Cd²⁺ blocking of the potassium conductance of TMHC6 and the E44H mutant. 3-fold higher Cd²⁺ concentrations were required to block the E44H mutant compared to the original design, likely because of the reduced electrostatic attraction. 3 cells were measured for each concentration and the mean (data points) and s.e.m. (error bars) are plotted. (c,d) Blocking of the conductance of the TMHC6 E44C mutant using cysteine reactive reagents. In panel (c), y axis shows the current amplitude and x axis indicates the time scale. Negatively charged MTSES, positively charged MTSET, and hydrophobic MTS-TBAE all completely blocked the ion conductance of the E44C mutant within a few minutes under voltage clamp control, while they had no effect on TMHC6 itself in control experiments. 9 cells for the control and 3 cells for each reagent were measured and the bars represent the mean of the measurements.

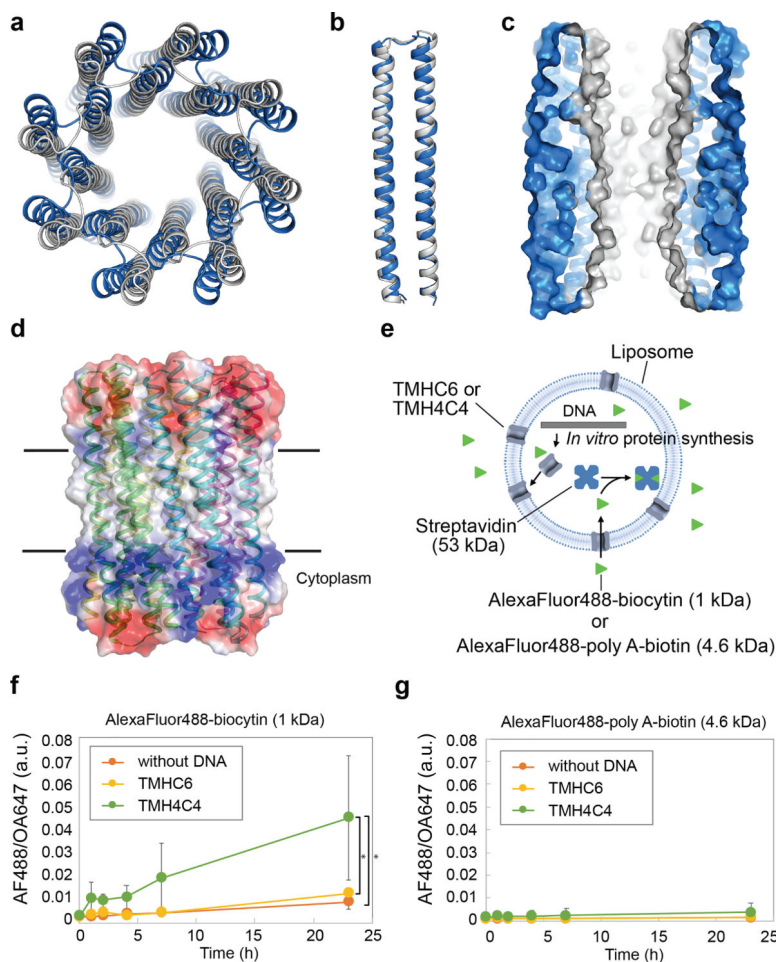


Figure 3. The X-ray crystal structure of water-soluble WSHC8 and the characterization of the 16-helix TMH4C4 transmembrane channel.

(a & b) Superposition of the full octameric assemblies and the monomeric subunits of the crystal structure (blue) and the design model (gray) of WSHC8. The C- α RMSD is 2.51 Å and 0.97 Å, respectively. The larger deviation for the octamer is caused by the slight tilting of the hairpin monomers along the superhelical axis of the complex. (c) The cross section of the WSHC8 channel. (d) TMH4C4 model with 16 transmembrane helices. The electrostatic surface of the neutral transmembrane regions is in gray. (e) Liposome permeability assay. Membrane channels are generated by *in vitro* translation inside streptavidin containing liposomes, biotin-labeled fluorescent dyes are added to the surrounding buffer, and the amount of dye trapped inside the liposomes is measured by flow cytometry. (f & g) TMH4C4 functions as a size-dependent transmembrane sieve. Incorporation of TMH4C4 into liposomes allowed the accumulation of the 1 kDa but not 4.6 kDa fluorescent dye, while TMHC6 disallowed both. Time courses of the median values of the histogram of Alexa Fluor 488/Ovalbumin conjugated to Alexa Fluor 647 (AF488/OA647) fluorescence (Extended Data Fig. 6e) which represents the concentration of the Alexa Fluor 488 inside the liposome are shown. For (f & g), the error bars indicate s.e.m. ($n = 7$; the means of the obtained median values are shown). Student's paired t-Test with a two-sided distribution was used to calculate the p values; * $p=0.0128$ (right) and 0.0220 (left). In control experiments

performed with α -hemolysin (AH) from *Staphylococcus aureus*, a well-studied channel forming protein³³ with a pore constriction of ~ 15 Å; only the smaller dye accumulated (Extended Data Fig. 6f–g), suggesting that, as intended, the assay measures solute passage through the transmembrane pores.

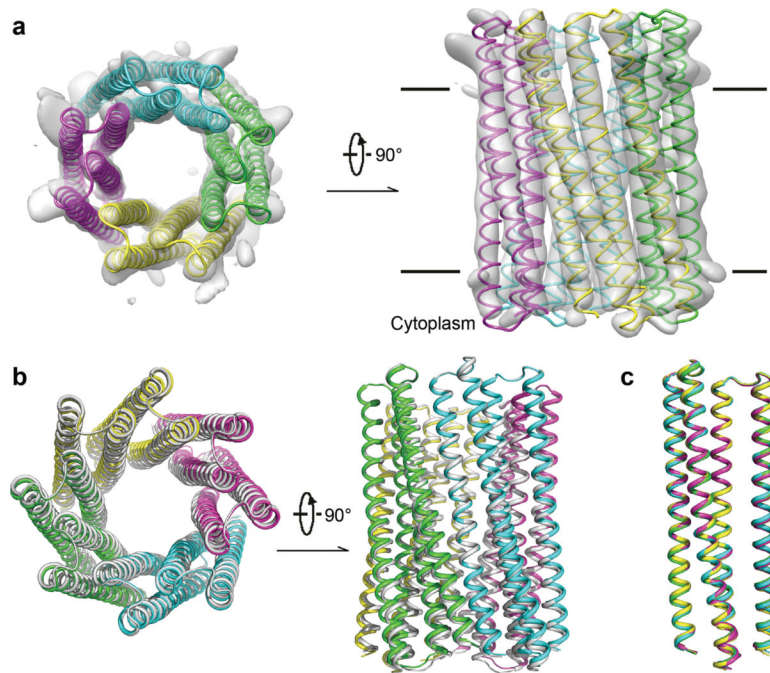


Figure 4. Cryo-EM of the 16-helix TMH4C4 transmembrane channel.

(a) Cryo-EM density (gray surface) and structure model (colored ribbon) of the 16-helix TMH4C4 protein. EM maps, generated in Chimera³⁴, are shown in two perpendicular views.

(b) Superposition of the cryo-EM structure (colored) and design model based on the crystal structure of the soluble form (gray) of TMH4C4.

(c) Structure alignment of the four protomers in one tetrameric cryo-EM structure of TMH4C4.